MEDICAL ROBOTS

An actuatable soft reservoir modulates host foreign body response

E. B. Dolan[1,2,3], C. E. Varela[1,4], K. Mendez[1,4], W. Whyte[1,5,6,7], R. E. Levey[3], S. T. Robinson[3,6,7], E. Maye[3], J. O'Dwyer[2,3], R. Beatty[3], A. Rothman[8], Y. Fan[8], J. Hochstein[4], S. E. Rothenbucher[1], R. Wylie[3], J. R. Starr[9], M. Monaghan[5,10], P. Dockery[3,11], G. P. Duffy[3,5,6,7,11]*†, E. T. Roche[1,8]*†

The performance of indwelling medical devices that depend on an interface with soft tissue is plagued by complex, unpredictable foreign body responses. Such devices—including breast implants, biosensors, and drug delivery devices—are often subject to a collection of biological host responses, including fibrosis, which can impair device functionality. This work describes a milliscale dynamic soft reservoir (DSR) that actively modulates the biomechanics of the biotic-abiotic interface by altering strain, fluid flow, and cellular activity in the peri-implant tissue. We performed cyclical actuation of the DSR in a preclinical rodent model. Evaluation of the resulting host response showed a significant reduction in fibrous capsule thickness ($P = 0.0005$) in the actuated DSR compared with non-actuated controls, whereas the collagen density and orientation were not changed. We also show a significant reduction in myofibroblasts ($P = 0.0036$) in the actuated group and propose that actuation-mediated strain reduces differentiation and proliferation of myofibroblasts and therefore extracellular matrix production. Computational models quantified the effect of actuation on the reservoir and surrounding fluid. By adding a porous membrane and a therapy reservoir to the DSR, we demonstrate that, with actuation, we could (i) increase transport of a therapy analog and (ii) enhance pharmacokinetics and time to functional effect of an inotropic agent. The dynamic reservoirs presented here may act as a versatile tool to further understand, and ultimately to ameliorate, the host response to implantable biomaterials.

INTRODUCTION

The long-term performance of implantable medical devices is drastically limited by complex and unpredictable foreign body responses (FBRs). Medical devices that depend on an interface with native tissue—such as neural probes (*1*, *2*), indwelling catheters (*3*), mammary implants (*4*), pacemakers (*5*), glucose biosensors (*6*–*8*), and drug and cell delivery devices (*6*, *9*–*12*)—are particularly vulnerable. These devices are often subject to a collection of biological host responses, such as fibrosis and inflammation, that can impair functionality. At present, device failure is expected and inevitable, and the costs, inconvenience, and morbidity that device failure can impose on patients are largely accepted. The implantable medical devices market is mature and growing (compound annual growth rate of 8%), with an estimated worth of about US$100 billion in 2019 (*13*). Implantable medical devices have various failure rates that can be attributed to fibrosis and can be as high as 30 to 50% for implantable pacemakers (*5*) and 30% for mammoplasty prosthetics (*4*). On the basis of a conservative rate of failure due to FBR of 10% for all implantable devices, the value of addressing this critical clinical need is US$10 billion per annum.

Once a device is implanted, a complex series of events is initiated to protect the host from the foreign body. Shortly after implantation, fibrinogen and other proteins bind to the surface of the device/foreign body; macrophages then bind and, over time, become multinucleated giant cells releasing inflammatory cytokines. In response to these signals, quiescent fibroblasts are transformed into myofibroblasts, which synthesize procollagen. The procollagen becomes cross-linked, and this mature cross-linked collagen and other extracellular matrix (ECM) proteins contribute to the formation of a dense fibrous capsule that becomes impermeable or hypopermeable to many compounds (*14*–*17*). This dense fibrous capsule can impair the function of implanted devices by obstructing diffusion (drug/cell delivery devices and biosensors) or causing capsular contracture (breast implants). Various strategies have been investigated to mitigate the FBR, such as generating scaffolds that release small molecules (*18*–*21*), modifying surface chemistry (*22*, *23*), and modifying implant size and geometry (*24*–*26*). However, these treatments have met with limited success because of difficulty in incorporating these modifications in a range of implantable devices.

There is a close relationship between macrophages and myofibroblasts during the fibrotic response, and both macrophages and myofibroblasts have been shown to be down-regulated when the fibrotic response to implanted alginate spheres is minimized (*25*, *27*). Macrophages have been shown to be a key driver of this down-regulated fibrotic response—depletion of the macrophage population resulted in a decreased fibrotic response (*25*, *27*). Strain, fluid agitation, and shear stress have been shown to influence the adhesion and proliferation of cells in vitro (*28*–*33*). Targeting cell activity with altered strain and fluid flow represents an innovative approach to modulating

[1]Institute for Medical Engineering and Science, Massachusetts Institute of Technology, Cambridge, MA, USA. [2]Biomedical Engineering, College of Engineering and Informatics, National University of Ireland Galway, Galway, Ireland. [3]Anatomy and Regenerative Medicine Institute (REMEDI), School of Medicine, College of Medicine Nursing and Health Sciences, National University of Ireland Galway, Galway, Ireland. [4]Harvard-MIT Program in Health Sciences and Technology, Cambridge, MA, USA. [5]Trinity Centre for Bioengineering, Trinity Biomedical Sciences Institute, Trinity College Dublin, Dublin 2, Ireland. [6]Advanced Materials and BioEngineering Research Centre (AMBER), Trinity College Dublin, Dublin, Ireland. [7]Royal College of Surgeons in Ireland, Dublin, Ireland. [8]Department of Mechanical Engineering, Massachusetts Institute of Technology, Cambridge, MA, USA. [9]Epidemiology and Biostatistics Core, The Forsyth Institute, 245 First Street, Cambridge, MA, USA. [10]Department of Mechanical and Manufacturing Engineering, School of Engineering, Trinity College Dublin, Dublin 2, Ireland. [11]CÚRAM, Centre for Research in Medical Devices, National University of Ireland Galway, Galway, Ireland.
*These authors jointly supervised this work.
†Corresponding author. Email: garry.duffy@nuigalway.ie (G.P.D.); etr@mit.edu (E.T.R.)

the FBR. We have shown in a previous study that extrinsic magnetic actuation of biphasic ferrogel scaffolds implanted in the proximity of injured muscle reduced fibrous capsule formation around the implant (*34*).

Soft robotic technologies are highly suited to medical applications involving human interaction because of their inherent conformability and ability to achieve biomimetic motion (*35*). Implantable soft robots represent a relatively unexplored frontier. These devices can be implanted in the body for an extended period of time and interact mechanically with tissues to regulate biological function. We have previously reported soft robotic cardiac assist devices that incorporate biomimetic actuation to emulate cardiac function to augment ventricular function in failing hearts (*36*–*38*). Here, we present a milliscale dynamic soft reservoir (DSR) that uses mechanical oscillation to modulate the biomechanics of the biotic-abiotic interface by perturbing fluid flow and cellular activity in the peri-implant tissue. We propose that this motion interferes with the progression of the FBR and endeavor to characterize this perturbation with in vitro and in vivo studies. Although we show one design of the DSR in this work, it represents a highly versatile and tunable dynamic platform that may be integrated into implantable devices to improve clinical outcomes or tuned as a research tool to further elucidate mechanisms of the fibrotic response to implanted materials.

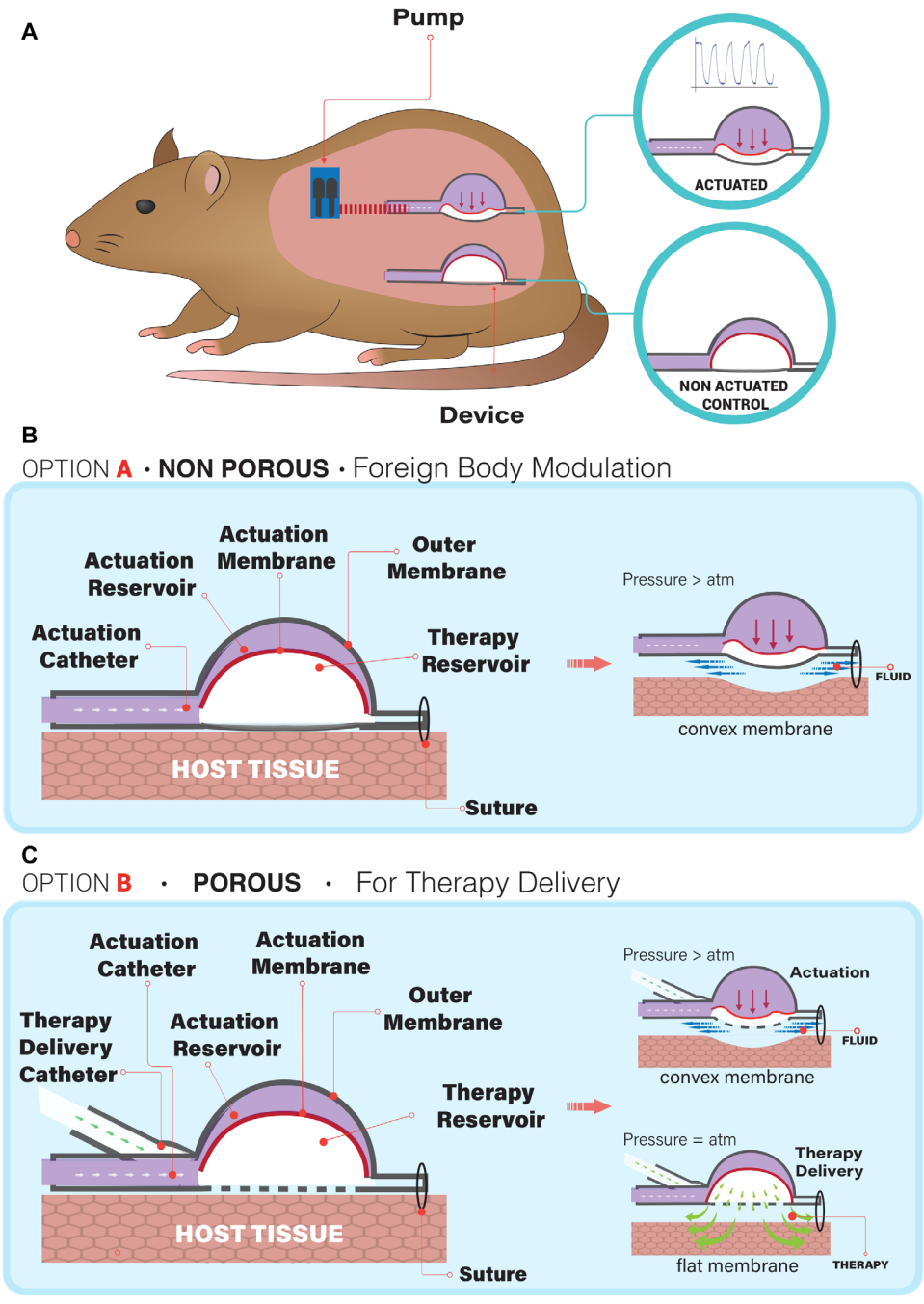

Fig. 1. An overview of the device and the proposed mechanism of action. (**A**) Implantable system showing a side-by-side implantation of a control and actuation group. (**B**) Nonporous configuration of the DSR for foreign body modulation for implantable devices. (**C**) Porous configuration of the DSR for therapy delivery.

RESULTS

Realization of DSR

In this work, we introduce an implantable pneumatically actuatable reservoir. The device can be cyclically actuated by an implantable pump, and we demonstrated this in a rat model (Fig. 1A, fig. S1, and movie S1). Cyclical pressurization results in a predictable, regime-specific deflection and strain of the lower functional membrane (Fig. 1, B and C). Multiple such reservoirs can be incorporated into a thin, conformable matrix that can be designed to be part of, or surround, implantable devices to reduce the host FBR (fig. S2). The proposed mechanism of action of the individual reservoirs is shown in Fig. 1 (B and C). When the actuation reservoir is pressurized through the actuation line, the volume and then pressure of the chamber increase. This causes a downward deflection of the middle and subsequently the lower membrane. Actuation causes deflection and strain of the membrane and results in fluid flow at the tissue interface (Fig. 1, B and C, blue arrows), which is proposed to interfere with cell activity and initiation of the fibrotic response. We propose two configurations of this device: one version with an impermeable, nonporous lower membrane (Fig. 1B), which would be incorporated in a sheath as a surface modification (suited toward implants with a structural role), and a second version with a permeable, porous membrane (Fig. 1C) that incorporates an additional

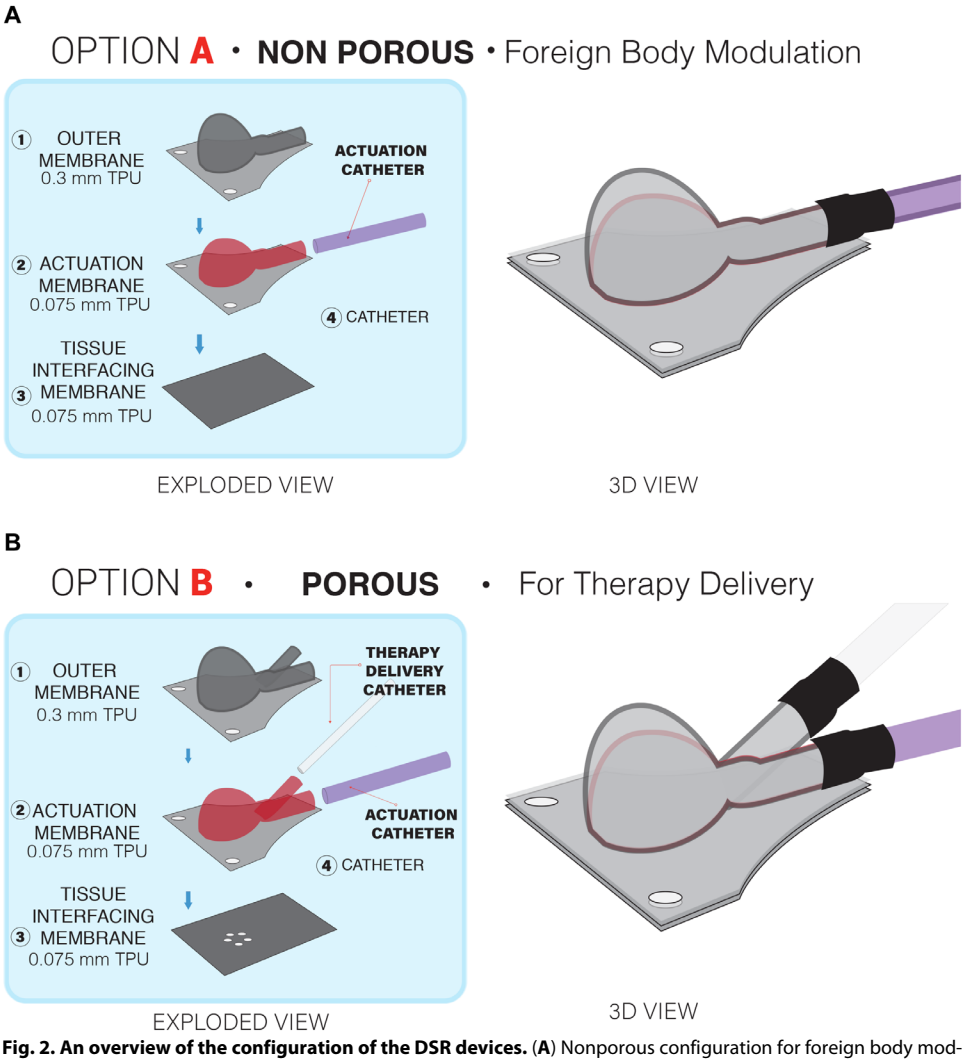

Fig. 2. An overview of the configuration of the DSR devices. (**A**) Nonporous configuration for foreign body modulation of implantable devices. (**B**) Porous configuration for therapy delivery.

therapy delivery line to the lower reservoir to allow transport of therapy into the tissue (suited for drug delivery or biosensing applications). The model DSR described in this work has a hemispherical shape (Fig. 2) with a 35-μl therapy reservoir, the size and shape of which was optimized for the delivery of cell-loaded biomaterials to the epicardial surface of the heart, as previously described (*39*). However, both the size and the shape of the DSR can be easily altered by modifying the positive and negative 3D-printed molds as shown in fig. S3. For example, a flat configuration of the DSR could be beneficial and could achieve the same deflection (see movie S2). An analytical model of this membrane deflection for a range of geometries is included in fig. S4.

Computational and experimental characterization of DSR

Pneumatic pressurization of the DSR alters its geometry, and the resulting deflection of the functional membrane causes localized changes to the mechanical environment and perturbations in the fluid flow in proximity to the device. To demonstrate this and to characterize the spatially varying stress and strain in the device, we conducted experimental materials characterization and computational modeling (Fig. 3). First, device materials were characterized. The thermoplastic polyurethane (TPU) used for the membrane (porous and nonporous) was tensile tested according to American Society for Testing and Materials (ASTM) D638. The resulting stress versus strain plots are shown in Fig. 3A. The data were fitted to a hyperelastic material model with the Ogden model being selected as the best fit (Fig. 3B and fig. S4). With this material model as an input, we created a finite element analysis (FEA) model to demonstrate the overall strain (Fig. 3C) and resulting stress (Fig. 3D) in the inner and outer reservoirs and membrane. This was repeated for the nonporous and porous membranes with maximum in-plane strains of 6.4 and 8.6%, respectively (fig. S4). To validate the computational models, we measured the force that the membrane applies to interfacing tissue, using a custom acrylic holder (Fig. S4) to consistently support the device in a materials tester, with the functional membrane in contact with the upper load cell. The cyclical forces for two regimes (regime 1 = 1 psi at 1 Hz, regime 2 = 2 psi at 1 Hz) were recorded, and peak forces were compared with each other and their corresponding FEA models, showing an excellent match between measured and predicted values (Fig. 3E). To further characterize the possible range of input pressures, we also modeled higher pressures and corresponding forces computationally and experimentally (Fig. 3F). A one-way analysis of variance (ANOVA) was performed with post hoc Tukey's test to compare the burst pressure of the devices after they were subjected to 100,000 cycles at pressures of regime 1 or regime 2. There was no statistical difference between regime 1 ($P = 0.7685$) or regime 2 ($P = 0.6251$) compared with the non-actuated control (Fig. 3G), indicating that the applied actuation regimes fell within the fatigue limit of the devices. We used a smoothed particle hydrodynamics model to quantify the fluid perturbations from device actuations during device actuation in fluid (Fig. 3, H and I) and an analytical model of a hinged plate to assess the sensitivity of the membrane deflection to design and actuation parameters (figs. S5 and S6). This study showed that pressure loading and radius size were both positively correlated to the deflection, whereas material stiffness and membrane thickness were negatively correlated to the deflection. Similar correlations were observed for the maximum radial strain and tangential strain (fig. S6). Although pressure loading was positively correlated with deflection in these analytical models, the differences in deflection between the pressures that we investigated in vitro and in vivo (1 and 2 psi for regime 1 and 2, respectively) are minor (~1% difference in strain and ~0.1-mm difference in deflection; fig. S6).

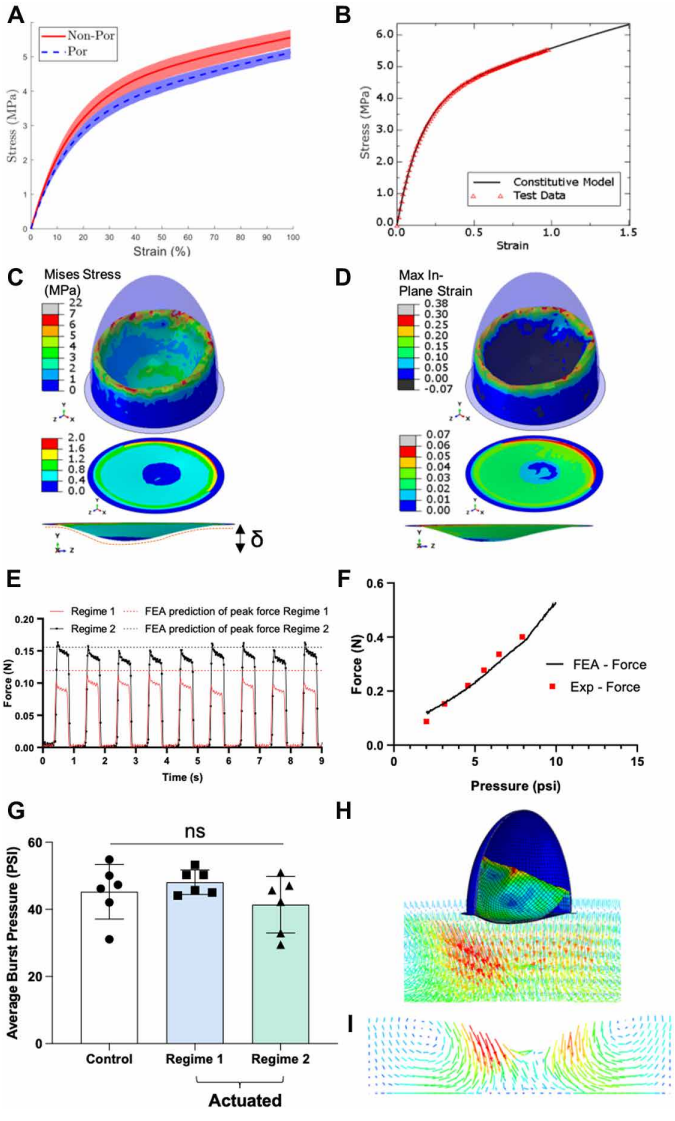

Fig. 3. Computational and experimental characterization. (**A**) Stress/strain plots for porous and nonporous thermoplastic urethane specimens. (**B**) Fitting of the porous data to the Ogden hyperelastic model. (**C**) Mises stress contour plots for the overall device, and the lower membrane (top-down and side view where the broken red line illustrates deflection, δ, of the membrane). (**D**) Maximum in-plane strain for the overall device and the lower membrane (top-down and side view). (**E**) Experimental cyclical force measurements of two actuation regimes (regime 1, 1 psi at 1 Hz; regime 2, 2 psi at 1 Hz), and finite element predicted force for each. (**F**) Relationship between input pressure and actuation force as measured experimentally and predicted with FEA. (**G**) Burst failure of DSRs after actuating at regime 1 or regime 2 for 100,000 cycles. $n = 6$ per group, data are mean ± SD, $P > 0.05$. (**H**) 3D smoothed particle hydrodynamic model showing the direction of fluid flow surrounding a DSR during actuation and (**I**) 2D slice of model to illustrate direction and magnitude of fluid flow at the area of maximum deflection.

To investigate the effect of actuation in vitro, we seeded the myofibroblast cell line WPMY-1 on the tissue-interfacing membrane of nonporous DSRs. DSRs were actuated (1 or 2 psi at 1 Hz for 5 min every 12 hours) for 14 days, and metabolic activity, cell viability, and soluble collagen production were compared with non-actuated controls. There was no significant difference between the two actuation regimes (1 and 2); for this and subsequent in vivo studies, we collapsed the variable and focused on analyzing the difference between control and actuated groups. We found that actuation did not significantly affect cell metabolic activity or viability compared with the non-actuated control and each time point (fig. S7, A to C). We show a downward trend in collagen production normalized by number of cells when comparing actuated to the controls (fig. S7D).

In vivo implantation of nonporous DSR reduces the FBR

To evaluate feasibility of the DSR to reduce the FBR in vivo, we first demonstrated that actuation forces were achievable with an implantable pump (Fig. 1A and fig. S1). Next, we implanted the nonporous DSR subcutaneously in a rat model (fig. S8), and we subjected the DSR to the actuation regime (Fig. 4A and movie S3) using a custom-built external control box (*36*, *38*).

On day 14, the devices were explanted en bloc with surrounding tissue and stained with phosphomolybdic acid (PMA) to enable visualization of collagen dense tissues. Images of the device and surrounding soft tissue were acquired using Scanco Medical MicroCT 100. Mimics (Materialise) software was used for segmentation of the device (Fig. 4B, shown in blue) and the fibrotic capsule present on the membrane of the device (Fig. 4B, shown in purple). Volumetric reconstructions of the fibrotic capsule were generated, and a thickness analysis was performed to identify mean capsule thickness. A significant reduction in the mean fibrotic capsule thickness was seen when the device was actuated compared with the control (***$P = 0.0005$, Fig. 4, C and D), and thickness dot plots of each animal are shown in Fig. 4E.

To characterize the effect of actuation on the cellular constituents involved in the FBR, we sectioned devices explanted on day 14 for histological analysis. Collagen fibers were characteristically birefringent, which was enhanced with Picrosirius staining. Polarized light microscopy was used to assess the quality and organization of the resulting fibrous capsule after staining. Quantification of birefringent fibers, using color threshold segmentation for mature fibers (red/orange) and immature fibers (green), yielded no statistically significant difference between groups ($P > 0.05$), irrespective of polarization color (Fig. 5, A and B) with an unpaired Student's t test. Quantification of the directional uniformity (coherency) of the collagen fibers showed no statistically significant difference in the fraction of fibers ($P > 0.05$, Fig. 5C) with an unpaired Student's t test, suggesting that actuation did not result in a compositional change in the collagen within the fibrous capsule.

Tissue sections were stained with CD68, a pan-macrophage marker, to assess the impact of actuation on the macrophage response at the tissue-device interface. Immunofluorescent images (Fig. 5D) were acquired for the control and actuated devices, and a stereological approach was used to provide a quantitative analysis of macrophage number (*40*–*42*). Numerical density was calculated (Fig. 5E) and referred to the number of, in this case, macrophages within a unit volume of tissue. A paired Student's t test was carried out with no statistically significant difference observed between groups ($P = 0.6963$), suggesting that actuation did not influence macrophage number at the device surface.

Immunofluorescent staining was also performed on the tissue sections for α–smooth muscle actin (αSMA) to assess for the presence of myofibroblasts around the control and actuated DSR (Fig. 5F). An unpaired Student's t test showed the total volume of αSMA-positive (αSMA^+) cells to be significantly lower with actuation compared

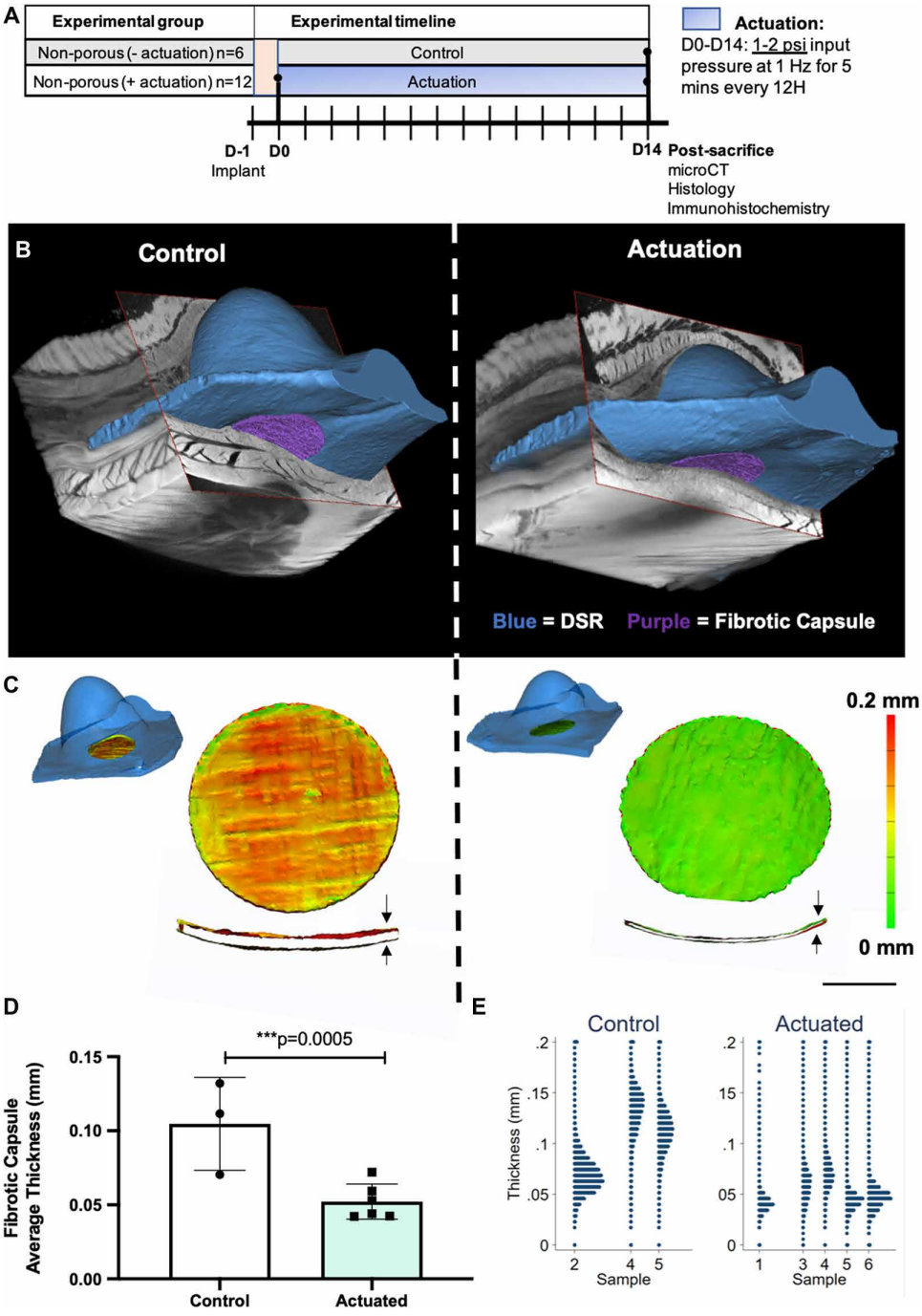

Fig. 4. DSR reduces the fibrous capsule thickness in vivo. (**A**) Timeline for in vivo studies for nonporous DSR. (**B**) Mimics reconstruction of soft tissue stained with PMA and imaged with microCT, where the DSR is shown in blue and the quantified segment of the fibrotic capsule is shown in purple. (**C**) Thickness analysis in Mimics where surface shell elements are shown, and thickness is calculated as the distance between them. (**D**) Average thickness across fibrotic capsule as measured by Mimics. (**E**) Dot plot of thickness measurement per sample (animal), n = 3 to 6 per group, data are means ± SD, ***P < 0.001.

with the control (**P = 0.0036, Fig. 5G). This suggests that actuation perturbed the number and likely the function of myofibroblasts in the fibrous capsule.

Neovascularization was also assessed in the fibrous capsule by staining for CD31 (Fig. 5H) and counting the number of vessels present around the control and actuated devices. Number per area and radial diffusion distance were all calculated using an unbiased counting frame (*41*–*43*). An unpaired Student's t test showed a significant increase in the number of $CD31^+$ blood vessels (**P = 0.0099, Fig. 5I) and a significant decrease in radial diffusion distance for the actuated DSR compared with the non-actuated controls (***P = 0.0009, Fig. 5J). This indicated an increased vascularity of the capsule after actuation.

In vivo enhancement of therapy delivery with a porous DSR

To investigate the transport of therapy through the resulting fibrous capsule, we injected a therapy analog Genhance (PerkinElmer) through the therapy delivery catheter of a control and actuated porous DSR and subsequently through the porous membrane to the surrounding tissue at days 8 and 14 (see Fig 6A for timeline). Fluorescent in vivo imaging was conducted for 1 hour after delivery of drug analog (Fig. 6B). Fluorescence (radiant efficiency) was plotted for each animal for 1 hour after delivery and for the control and actuated DSR, and the area under the radiant efficiency curve was calculated (Fig. 6C). There was a decrease in the amount of drug analog delivered to an area of tissue surrounding the implant over time, as expected due to the attenuation of drug diffusion caused by the FBR (Fig. 6C). However, the actuated devices delivered more drug analog compared with the control at each time point (37 and 16% mean improvement at days 8 and 14, respectively; Fig. 6C). The area of diffusion was also quantified with the actuated groups showing a larger spatial area of diffusion [in a two-dimensional (2D) plane] than the control after 1 hour at days 8 and 14 (Fig. 6D).

Demonstration of functional effect due to enhanced delivery through an actuated DSR

As a model therapy to visualize rapid drug delivery, epinephrine was delivered through the control and actuated devices (n = 1). Using a pressure-volume catheter, we measured the maximum rate of change of the interventricular pressure (dP/dt max is a measure of the contractility of the ventricle) immediately after delivery of the drug. The time to therapeutic effect is defined as the time when the dP/dt max leveled off and stopped increasing. This time is indicated by dashed lines for a control

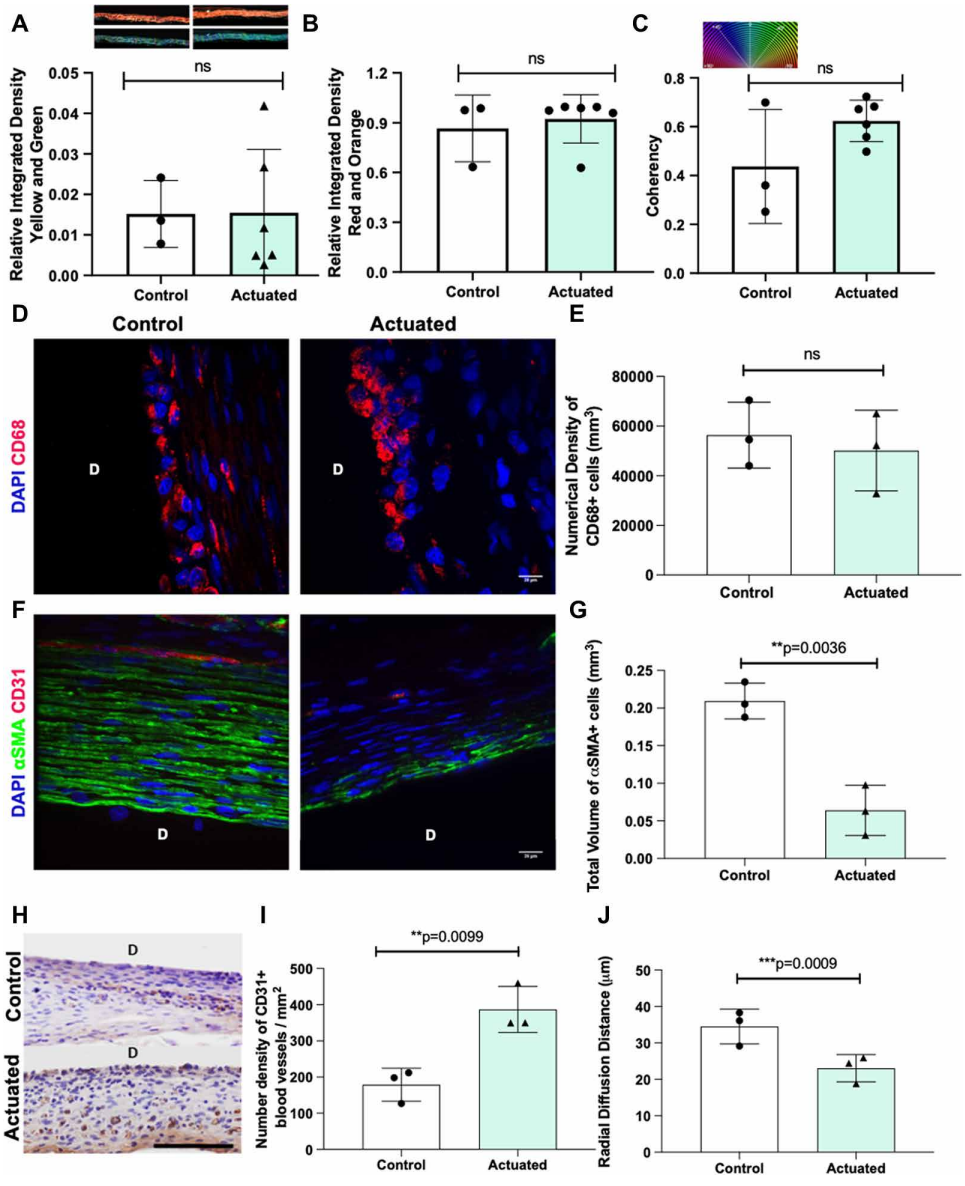

Fig. 5. Histological analysis of the fibrous capsule. (**A**) Relative integrated density of yellow and green fibers (signifying immature collagen) from polarized light microscopy images of the fibrous capsule in response to different treatments, with representative images shown. (**B**) Relative integrated density of red and orange fibers (signifying mature collagen) from polarized light microscopy images of the fibrous capsule. (**C**) Coherency of fibrous capsule based on polarized light microscopy. (**D**) Representative immunofluorescent images of capsular tissue sections stained with CD68 (red, CD68; blue, Hoechst). (**E**) Numerical density of CD68-stained macrophages in different treatment groups. (**F**) Representative immunofluorescent images of capsular tissue sections stained with αSMA [blue, DAPI (4′,6-diamidino-2-phenylindole); green, αSMA; red, CD31]. (**G**) Total volume of αSMA$^+$ cells (mm^3). (**H**) Representative images of capsular tissue sections stained with CD31. (**I**) Number of blood vessels per square millimeter. (**J**) Radial diffusion distance for regime 2 compared with control. D, device; n = 3 to 6 per group; data are means ± SD; $^{**}P < 0.01$, $^{***}P < 0.001$.

changes to the TPU material or overall device when submerged for up to 1 week in hypotonic and hypertonic solution in vitro.

DISCUSSION

In this study, we describe milliscale DSRs that use a mechanoceutical approach to actively modulate the biomechanics of the biotic-abiotic interface by perturbing strain and fluid flow. We show, using computational and experimental techniques, that the DSR created strains of 6.4 and 8.6% on the nonporous and porous membranes at a pressure of 2 psi and thereby induced peri-implant fluid flow in close proximity to the device. A parametric study shows the tunability of the platform and that pressure loading and radius size were both positively correlated to the deflection, whereas material stiffness and membrane thickness were negatively correlated to the deflection. In a 14-day rat study with a nonporous DSR, we show a significant reduction in fibrotic capsule thickness with no statistical difference in capsule quality (collagen maturity and coherency). We also show a reduction in αSMA myofibroblasts, an increase in the number of CD31$^+$ neo-vessels, and a decrease in radial diffusion distance between CD31$^+$ vessels in the actuation group compared with non-actuated controls. We demonstrate that this reduction in FBR could cause enhanced pharmacokinetics in a porous DSR incorporating a drug delivery component, where we show an improvement in the amount and the area of diffusion at days 8 and 14. To demonstrate a functional effect with a model pharmacological agent, we delivered an inotropic drug, epinephrine, through a porous DSR, and show that we could increase cardiac contractility and develop pressure more efficiently and quickly in the actuated group compared with the control, likely due to the reduced fibrous capsule in the actuated DSR.

This implantable device uses the principles of soft robotics to cyclically actuate a flexible membrane that modulates the biomechanics of the biotic-abiotic interface. This approach takes advantage of controlled mechanical actuation to elicit a specific biological response and, as such, reduces fibrotic encapsulation of implantable medical devices. An unwanted 50- to 200-μm-thick fibrotic capsule has been reported to build up (<1 month) and envelop implanted devices (*25*, *44*), which can be detrimental to the function of the device and cause significant pain

and actuated device in the same animal (Fig. 6E) and is lower (~40 s) for the actuated device compared with the control (~170 s). The cyclical average dp/dt max in the first 40 s after delivery was significantly higher ($P < 0.0001$) in the actuation group compared with the control (Fig. 6F), acting as a clinically responsive model to demonstrate enhanced delivery after the actuation regime. Last, an osmolarity study (fig. S9) demonstrates that there were no significant dimensional

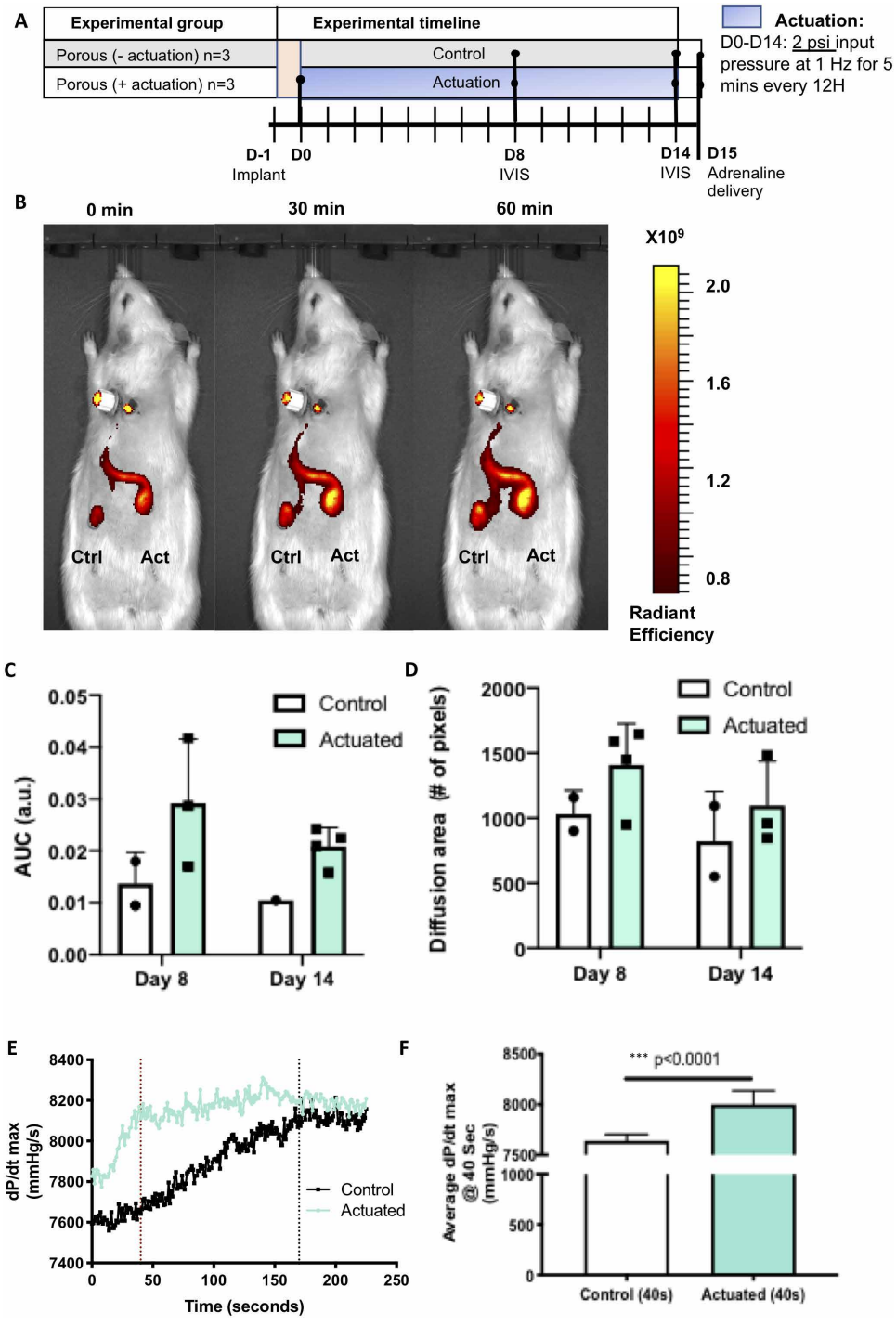

Fig. 6. Enhanced pharmacokinetics through a porous DSR with actuation. (**A**) Timeline for in vivo studies for porous DSR. (**B**) Images from the IVIS at day 14 at 0, 30, and 60 min showing the implanted actuation and control groups. (**C**) Area under the fluorescence curve at days 8 and 14 for actuated and control groups, $n = 2$ to 4 per group per time point, data are means ± SD. (**D**) Diffusion area at days 8 and 14 for actuated and control groups, $n = 3$ to 4 per group per time point, data are means ± SD. (**E**) *dP*/*dt* max, a measure of ventricle contractility for the actuated and control DSRs in a representative animal. The vertical dashed lines show time to therapeutic effect for the control and actuated groups. (**F**) Average *dP*/*dt* max per cycle for the first 40 s (the time to therapeutic effect for the actuated group). Ctrl, control; Act, act; AUC, area under the curve; a.u., arbitrary units.

and discomfort to the patient (*44*, *45*). The fibrous capsule thickness reported in this study for the non-actuated control falls within this range (control, 0.1047 ± 0.0314 mm), whereas we show a significant ~2-fold reduction in thickness with actuation (actuated, 0.05218 ± 0.0151 mm, $^{***}P = 0.0005$). We show that there was no statistical difference in the collagen content of the resulting fibrous capsule ($P > 0.05$), meaning that we report a thinner capsule with no difference in quality.

Macrophages have been shown to be a key driver of the fibrotic response (*25*), and strain has been shown to modulate macrophage polarization to proinflammatory or prohealing phenotypes (*33*). In this study, computational models predict maximum strain levels of 6% on the functional membrane of the reservoir, which is below the strain shown to cause macrophage detachment (12%) (*33*). In agreement with this, we found no biologically relevant difference in the numerical density of macrophages at the interface when quantified by CD68 staining in the actuation group compared with the control (45,417 ± 16,799 versus 67,024 ± 23,976, $P = 0.6983$). The maximum strain predicted in this study (6.4% for nonporous membranes and 8.4% for porous membranes) is similar to results by Ballotta *et al.* (*33*), who showed activation toward the prohealing (M2) phenotype at 7% strain, which may potentially explain the reduced fibrous capsule thickness we report. Strain and fluid flow are also known to have distinct effects on fibroblasts and myofibroblasts during healing processes (*46*). Cyclic mechanical loading has been shown to reduce myofibroblast differentiation of primary lung fibroblasts (*47*), and growth and repair processes of the heart are guided by mechanical stimuli (*48*, *49*). These results suggest that actuation may be a potential mechanistic target to modulate ECM synthesis in fibrotic capsule formation and contracture. Here, we show a significant reduction in the number of αSMA^+ myofibroblasts ($P = 0.0036$) with no change in $CD68^+$ macrophages ($P = 0.6963$) in the actuated group compared with the control, and we propose that actuation-mediated strain of the cells present in the capsule reduces differentiation and proliferation of myofibroblasts and therefore

ECM production and overall capsule thickness. Our in vitro investigation of the WPMY-1 myofibroblast cell line shows that actuation did not significantly affect metabolic activity or cell viability and resulted in a downward trend in collagen production per cell. However, it is difficult to recapitulate innate host responses at a single in vitro cellular component level because the complex signaling environment between macrophages, myofibroblasts, and many other cells during the fibrotic cascade is not captured. For this reason, we focused on the in vivo outcomes in this study. Although the bulk in-plane strains shown in this study may not be experienced at the cellular level initially, mechanical forces and strains will be transduced as a connected fibrous capsule matures around the implant.

In a previous study, we reported a replenishable implanted epicardial reservoir and showed that, despite the formation of a fibrous capsule (which hinders but does not impede diffusion), molecules with a range of molecular weights could be transported through the membrane into the tissue (*39*). In this study, we show an improvement point (37 and 16% mean improvements at days 8 and 14, respectively) in diffusion of a therapy analog through the fibrous capsule compared with the control. This improvement in diffusion is particularly important in the field of cell and drug delivery to treat type 1 diabetes, specifically for cell encapsulation strategies where rapid diffusion of glucose and insulin is required (*50*, *51*). Modified alginate spheres encapsulating stem cell–derived β cell have been shown to reduce fibrosis and result in long-term glycemic control in mice (*22*, *23*, *25*). The replenishable nature of the therapeutic DSR, with a reduced FBR after actuation, offers a number of advantages over biomaterial encapsulation because it allows for (i) top-up and refill, (ii) multiple dose forms, and (iii) multicargo delivery that can be tailored to patient need.

There are some limitations with the current study. Here, we list these shortcomings and suggest further steps that need to be taken to realize clinical translation of the DSR. First, our sample sizes for this proof-of-concept study were small, and therefore, the study is more of a demonstration that a dynamic reservoir can affect host response than a preclinical study designed for a specific clinical application. Longer-term in vivo studies with increased sample sizes will be required to study the long-term effects of this kind of therapy, including how responses change once actuation ceases. For moving toward clinical translation, we aim to use a refined implantable pump (Fig. 1A, fig. S1, and movie S1). Ultimately, we plan to power and control this pump using wireless technology. Second, more complex, closed-loop interactions with the host could be added, for example, triggering actuation when the implant senses specific cellular activity on the functional membrane. Leveraging the ongoing miniaturization of sensors (*52*, *53*), the continuing evolution of techniques for wireless communication and power transfer (*54*, *55*), and energy scavenging (*56*) will allow us to modify the device to achieve this control.

In conclusion, this work demonstrates the ability for dynamic implantable devices to affect the host response to medical implants. We show two configurations of this strategy to demonstrate the potential of this device. The impermeable, nonporous configuration could be incorporated in a sheath as a surface modification for implants with a structural role, such as breast implants and pacemaker leads, preventing capsular contraction. The permeable, porous configuration improved the transport of therapy into the tissue, which is desirable for drug/cell delivery or biosensing applications. As such, we suggest that these soft, mechanoceutical devices may lead to a myriad of implantable, application-specific soft robots specifically designed to study or treat clinical conditions. If we can harness this phenomenon to address clinically adverse issues that are commonplace with implanted devices, then the strategy can lead to opportunities for the field of soft robotics in fine-tuning the biological host response.

MATERIALS AND METHODS

Study design

The overall objective of the study was to demonstrate that actuation of an implantable reservoir (DSR) modulates the FBR. Our control group was a static implanted DSR, and our treatment group was an actuated DSR (actuated to 1 to 2 psi for 5 min every 12 hours for 14 days). We conducted an in vitro study with control and treatment DSRs seeded with a myofibroblast cell line and analyzed cell viability, metabolic response, and collagen deposition with lactate dehydrogenase (LDH) cytotoxicity assay, alamarBlue metabolic activity assay, and Sircol soluble collagen assay, respectively. A time point of 14 days was used on the basis of previous studies assessing fibrotic encapsulation of materials (*25*, *27*). We then conducted two in vivo studies. The first was with a nonporous version of the DSR with the objective of measuring fibrous capsule thickness, quality, and composition. We implanted two devices per animal, with a sample size of 3 to 6. Control and treatment groups were paired as far as possible to enhance statistical power, given the low sample size. To measure thickness, we conducted microcomputed tomography (microCT) analysis with subsequent thresholding and segmentation in Mimics software (Materialise). Up to 4000 measurements of the thickness of the fibrous capsule were made, and analysis was repeated by two blinded operators. We then conducted immunohistochemistry for macrophage content and blood vessel content. Again, two blinded counters were used for each analysis. For the second in vivo study, we used a porous version of the DSR, with the objective of measuring the amount of drug delivered through an actuated and control DSR at days 8 and 14 after implantation to assess whether the decreased fibrous capsule affected cargo delivery through the device. We used the therapy analog Genhance and measured the amount of analog delivered and the spread of the drug in each group by quantifying fluorescence at days 8 and 14. Again, a sample size of 3 to 6 was used. The control and treatment groups were paired within animals, where possible, to allow paired statistical analysis. We then did a proof-of-concept study with one animal to show that a pharmacological agent (epinephrine) could diffuse through the capsule and that this exerted its action more rapidly in the treatment group.

DSR fabrication

The device manufacture technique for the individual reservoirs is shown in fig. S3. Briefly, 0.075- and 0.3-mm-thick TPU sheets (HTM-8001-M and HTM-1001 polyether TPU film, American Polyfilm, Inc.) were formed into hemispherical shapes, with a height of 3.9 mm and a diameter of 3.5 mm, using a vacuum thermal former (Yescom Dental Vacuum Former, Generic). TPU hemispheres (0.075 mm thick) were placed inside the 0.3-mm-thick TPU hemispheres, and 7 cm of 3 Fr TPU catheter tubing (0.037″ × 0.023″; MRE037, Micro-Renathane, Braintree Scientific) was bonded to this assembly using a heat transfer machine (QXAi, Heat Transfer

Machine, PowerPress). This formed the actuation reservoir, which was used for actuating the system with pneumatic pressure via the catheter. A 0.075-mm-thick TPU membrane and a second 9-cm 3 Fr TPU catheter were then bonded onto this assembly to form the therapy reservoir, which could be used to deliver therapeutics before or after implantation via the catheter. This reservoir interfaced with soft tissue via the TPU membrane, which could be either nonporous or porous (Fig. 1B). Ten-micrometer pores (National Centre for Laser Applications, National University of Ireland Galway) were used in this study to minimize fluid flow into the DSR therapy reservoir during actuations. The size and shape of the DSR can be easily altered by modifying the positive and negative 3D-printed molds as shown in fig. S3.

Implantable system

A fully implantable peristaltic pump (Dolomite 3200243) was used for cyclic actuation of DSRs. The device was placed in series with the outflow tube of the pump. A TinyLily mini processor (ASM2101, TinyCircuits) and TinyLily motor board (ASL2001, TinyCircuits) connected via a custom printed circuit board (OSH Park) were used to regulate pumping. The entire assembly was powered by a small 3.7-V lithium ion battery (2011 Adafruit). Running a customized program written in Arduino, the control system can turn the pump on for an adjustable period of time and then reverse the direction of electric current, causing it to pump in reverse for another adjustable time interval. Calibration of the forward/reverse cycles enabled cyclic actuation at a variety of desired pressures and peak forces. We tuned the force and frequencies to match that of the external control box and measured the cyclical force with an Instron 5944 materials testing machine (fig. S1).

Experimental characterization of the DSR

Uniaxial tensile tests (according to ASTM D638) were performed on a ZwickRoell material testing machine with laser-cut TPU specimens. Using the material evaluation feature in Abaqus 2018 (Dassault Systèmes, Vélizy-Villacoublay, France), we evaluated four hyperelastic constitutive models (Neo-Hookean, Yeoh, Mooney-Rivlin, and Ogden third order). As shown in Fig. 3B, the Ogden third-order model had excellent curve fitting performance and therefore was used for the model. The strain energy density function is shown in fig. S5C. The actuation force of the device was measured using an Instron 5944 material testing machine. The setup is shown in fig. S5. An acrylic test rig (fig. S5) was laser cut to allow the lower membrane of the device to contact the upper compression plate for force measurement. The thickness of the acrylic piece (10 mm) and the diameter of the hollow cylinder (5 mm) were designed to be larger than the height and the diameter of the outer membrane, allowing unconstrained deformation of the reservoir. The distance between the compression plates was fixed at the thickness of the acrylic holder. The force was measured using a 50-N load cell. To test the effect of fatigue on the devices, we applied 100,000 cycles at 1 and 2 psi at 1 Hz to nonporous DSR in vitro and carried out burst pressure testing (n = 6 per group). A pressure sensor (TruWave intravascular disposable pressure sensors, Edwards Lifesciences) with an amplifier (instrument amplifier INA125P, Digi-Key) and an Arduino UNO interface was connected to the device and syringe via a T valve. A syringe pump (PHD ULTRA, Harvard Apparatus) was used to inflate the devices to failure, and burst pressure was recorded.

Computational modeling

All simulations were conducted in the commercially available software, Abaqus 2018 (Dassault Systèmes, Vélizy-Villacoublay, France). Because the reservoir is composed of thin TPU sheets, shell structural analysis was chosen for the simulation. The device was modeled as a 3D surface geometry, which contains the outer, middle, and lower membranes, as shown in fig. S5. The appropriate thickness of each shell was assigned. All parts were meshed with 2603 four-node shell elements (S4R). Dirichlet boundary condition was applied to the protruding edge of the lower membrane, and all other surfaces were allowed to deform freely. A 2-psi ramp loading was applied to the internal surface of the inner and outer membranes for a duration of 500 ms. These boundary conditions were representative of the in vivo scenario when the reservoir was sutured to the muscular tissue by the edge of the lower membrane and actuated with a cyclic pressure with a magnitude of 2 psi and 1 Hz.

We also created a fluid structure interaction model using the smooth particle hydrodynamics technique to study the effect of actuation on surrounding fluid flow (Fig. 3, H and I). A 20-mm–by–20-mm–by–5-mm region was created and filled with 8000 particles. The particles were assigned a density of 9.96×10^{-7} kg/mm^3, a bulk modulus of 20.94 MPa, and a dynamic viscosity of 3.56×10^{-8} MPa.s. Contact pairs were initiated between the shell structure and the particles. Loading and boundary conditions of the shell were the same as the structural analysis.

In vitro studies

The WPMY-1 myofibroblast cell line (ATCC CRL-2845) was cultured in high-glucose Dulbecco's modified Eagle's medium D5671 (Sigma) supplemented with 5% fetal bovine serum (FBS), 1% penicillin-streptomycin, and 0.05% L-glutamine. The nonporous membranes of the DSR were soaked in 150 μl of FBS for 2 hours. The FBS was then washed off with phosphate-buffered saline (PBS), and myofibroblasts were seeded on the nonporous membranes of the DSRs at 25,000 cells per device and cultured for 24 hours (37°C, 5% CO_2). The DSR was actuated to 1 or 2 psi at 1 Hz for 5 min every 12 hours for 14 days, and metabolic activity, cell viability, and soluble collagen production were compared with non-actuated controls at days 3, 7, 10, and 14. Metabolic activity was assessed using alamarBlue assay as previously described (*57*), cell viability was assessed using LDH cytotoxicity assay, and collagen production was assessed using Sircol soluble collagen assay following the manufacturers' protocols. Devices were fixed with 4% paraformaldehyde for 10 min and then washed three times in 1× PBS before permeabilization of the cells with 0.15% Triton X-100 in 1× PBS for 2 min. Devices were washed three times in 1× PBS and blocked in 1% bovine serum albumin (BSA) for 30 min before staining with Alexa Fluor 488 Phalloidin (catalog no. A12379, Thermo Scientific) at 1:200 dilution for 60 min. Devices were washed three times in 1× PBS before counter staining with Hoechst at 1:1000 dilution for 10 min. Devices were then mounted using fluoromount (F4680, Sigma) and observed using a spinning disc inverted confocal microscope (CSU22, Yokagawa) combined with Andor iQ 2.3 software.

In vivo studies

Animal procedures were reviewed and approved according to ethical regulations by the Institutional Animal Care and Use Committee at Massachusetts Institute of Technology. Female Sprague Dawley rats (225 to 300 g) were anesthetized using isoflurane (1 to 3% isoflurane

in oxygen). Animals were treated with a single dose of sustained-release buprenorphine (Bup-SR) at 1 mg/kg subcutaneously to control pain. Two DSR devices (porous or nonporous) were implanted subcutaneously in the rat; the device implantation procedure is shown in fig. S8. Briefly, the hair on the back of the rat was removed, and surgical sites were prepared with three washes of Betadine and 70% ethanol. Devices were sterilized using ethylene oxide before implantation. An anterior incision was made at the base of the neck for the port, and two posterior incisions were made 9 cm from the original incision along the back of the rat and 1 cm lateral of the spine. A blunt dissection was made at all incisions, and a pair of forceps was used to tunnel subcutaneously from the anterior to the posterior sites. A vascular access button, or self-sealing subcutaneous port (VAB95BS-MRI, VABM2B/22R22, VABR4B/22 Instech Laboratories), was connected to the dorsal end of the catheter of each DSR. The port was placed in position at the base of the neck, and the devices were tunneled posteriorly into position. The port was secured to the underlying fascia using at least one interrupted suture (5-0 monofilament). Each DSR was secured to the underlying fascia with one suture at either side (7-0 monofilament). The skin was closed with interrupted sutures (5-0 monofilament), and the animal was allowed to recover on a heated pad. Three milliliters of warm saline was administered subcutaneously. The following day, one of the two implanted DSR devices was actuated at controlled input pressures of 1 psi (regime 1) or 2 psi (regime 2) at 1 Hz every 12 hours for 14 days (Fig. 5A and fig. S7A) and compared with the non-actuated control reservoir for analysis. On day 14, animals were euthanized by CO_2. After euthanasia, each device and the immediate surrounding tissue were extracted. Tissues were fixed for 24 hours using 10% formalin (pH 7.4). The tissue was then washed in 0.2 M PBS with a final wash in 70% ethanol.

IVIS imaging

On days 8 and 14, diffusion of a fluorescent imaging agent (Genhance 750 Fluorescent Imaging Agent, NEV10118, PerkinElmer) out of the porous DSR devices was evaluated using an In Vivo Imaging System (IVIS) Spectrum-bioluminescent and fluorescent imaging system (PerkinElmer). Images were acquired using a 745-nm/800-nm excitation/emission filter pair. Before injection of the agent, the line was cleared by establishing vacuum with a syringe connected to the subcutaneous port. The skin above the DSR area was shaved and marked to aid with region of interest (ROI) placement for quantitative analysis. After a background image was acquired, 35 μl of fluorescent agent was injected through the subcutaneous port either manually or with a syringe pump (150 μl/min; Harvard Apparatus). Images were acquired for up to 1 hour after injection about every 3 min. An ROI (28.24-pixel-diameter circle) was placed at the center of each DSR in each image, and the total radiant efficiency was measured using Living Image 3.2 software. The total radiant efficiency measured immediately after injection was subtracted from the subsequent measurements to account for the change in radiant efficiency due to diffusion over time. For the measurement of diffusion area, the color ranges of IVIS images obtained immediately after injection and after 1 hour of diffusion were adjusted such that delineation of the areas of interest was possible. The adjusted image files were imported into ImageJ, and the corresponding diffusion areas were delineated using the polygon tool and quantified. The area measured immediately after injection was subtracted from the area measured after diffusion.

Functional measurements following epinephrine injection

To illustrate how actuation can improve the time to functional effect after small-molecule delivery, we delivered 35 μl of epinephrine (1 mg/ml) through the porous DSR while recording blood pressure with an apically inserted pressure-volume catheter (Millar) and PowerLab (ADInstruments) as previously described (*39*). Using the pressure-volume data and the pressure-volume module in LabChart software (ADInstruments), we plotted dP/dt max, an index of contractility over time for 10 min after injection for a control or actuated device.

microCT, histological, and immunohistochemical analysis

For microCT analysis, fixed tissue samples were transferred to a 2.5% PMA solution in 70% ethanol for 7 days, then washed, and stored in fresh 70% ethanol. MicroCT images were captured using a microCT 100 scanner (Scanco) at 70 kVp and 85 μA with a 0.5-mm aluminum filter. microCT DICOM (Digital Imaging and Communications in Medicine) files were segmented using Mimics Research 18.0.0.525 software (Materialise) as described in the Supplementary Materials.

Fixed tissue samples (n = 3 to 6 animals per group) were transected in half, oriented, and embedded in paraffin wax blocks for histological and immunohistochemical analysis. Sections of 5 μm were cut, deparaffinized in xylene, and rehydrated through a series of graded alcohols. For histological fibrotic capsule quality analysis, sections were stained with 0.1% Picrosirius red/fast green solution (1:1) using an automated stainer (ST5010 Autostainer XL, Leica). Slides were imaged using Oculară 2.0 Imaging Software on an Olympus BX41 Microscope with Olympus U-AN360P analyzer under a 20× objective lens. Quantification of the collagen content was performed using a previously reported technique (*58*, *59*). For immunohistochemical analysis, primary antibodies of CD31 (1:200; ab28364, Abcam), CD68 (1:300; MCA341, Bio Rad), and αSMA (1:100; ab5694, Abcam) were incubated for 1 hour at 37°C. Secondary antibodies of Alexa Fluor 594 goat anti-mouse immunoglobulin G (IgG; 1:200 Thermo Fisher Scientific), Alexa Fluor 594 goat anti-rabbit IgG (1:200; Thermo Fisher Scientific), and Alexa Fluor 488 goat anti-mouse IgG (1:200; Thermo Fisher Scientific) were incubated for 60 min at room temperature, respectively. Sections were stained with Hoechst and coverslipped using fluoromount. Immunofluorescence-stained slides were observed using a spinning disc inverted confocal microscope (CSU22, Yokagawa) combined with Andor iQ 2.3 software.

Analysis of macrophages

Twenty random fields of view were acquired from eight sections using confocal microscopy. Using stereological methods, an unbiased estimation of area fraction and numerical density (Nv) was calculated (*40*–*42*). Numerical density refers to the number of, in this case, macrophages within a unit volume of tissue.

Analysis of myofibroblasts

Twenty random fields of view were acquired from eight sections using confocal microscopy. Area fraction was estimated using ImageJ (Fiji verson 2.0.0) software. This was done by way of auto thresholding using the otsu filter, which eliminates autofluorescence and calculates the area fraction of tissue occupied by αSMA^+ cells. The area fraction was then multiplied by the average volume of the region of interest in both control and regime groups to provide an estimate of the total volume of αSMA^+ cells to assess whether the presence of myofibroblasts was perturbed by actuation.

Analysis of neo-vascularization

Number per area (Na) and radial diffusion distance (Rd) were calculated using an unbiased counting frame (*41*–*43*). This counting frame consists of red forbidden lines and green acceptance lines. Any blood vessel that was cut by a forbidden line was not counted. Blood vessels that appeared outside the counting frame or were cut by the acceptance lines without also cutting the forbidden line were counted. The application of this counting formula generates an unbiased estimate of the number of blood vessels per unit area. Na= cN/(cPts × area of grid) taking cN as the cumulative number of blood vessels counted and cPts as the cumulative number of points. The length density (Lv) of a blood vessel is the length of blood vessels present per unit volume and was calculated by multiplying the numerical density by 2. From Lv, the radial diffusion distance (Rd) can be calculated by the following formulas: $Lv = Na \times 2$, $Rd = 1/\sqrt{[\pi(Lv)]}$.

Statistical analysis

GraphPad Prism (8.1.0) or Stata version 16.0 was used for statistical analysis. Nonparametric tests were sometimes performed for $n \leq 3$ per group, in part because the sample was too small to test whether the endpoint was normally distributed. However, the *t* test is fairly robust to departures from normality, and in many circumstances, it is more powerful than corresponding nonparametric tests (*60*). Thus, we conducted *t* tests (or generalizations of *t* tests, as we explained) to compare endpoint measurements between the control and actuated samples. Where possible, when each animal had both a control and an actuated device, we used paired *t* tests. For endpoints for which some animals had data only under control or only under actuated conditions, we fitted linear regression models in a generalized estimating equations (GEE) framework, with robust standard errors and an independent correlation structure (*61*). The GEE model can be thought of as being similar to the paired *t* test while allowing an unbalanced design and accounting for the correlated data caused by having control and actuated measurements in the same animals. To maximize study sensitivity, we considered the primary analysis to have only two comparison groups; i.e., we collapsed data from regimes 1 and 2 into one treated group (actuation). We consider the comparison of measurements between two regimes (e.g., two different pressure levels) as exploratory; i.e., we do not consider the *P* value a dichotomous significance test. For burst pressure and osmolarity analyses, there were more than two groups. First, normality was tested with a Shapiro-Wilk test; if the data were normally distributed, we used a one-way or two-way ANOVA with Tukey's post hoc adjustment for multiple comparisons. If the data were not normally distributed, a Kruskal-Wallis test was used with Dunn's post hoc adjustment for multiple comparisons. Statistical significance was accepted when $P < 0.05$.

SUPPLEMENTARY MATERIALS

robotics.sciencemag.org/cgi/content/full/4/33/eaax7043/DC1
Materials and Methods
Fig. S1. Implantable actuation system.
Fig. S2. Nonporous DSR arrays to reduce complications associated with implantable devices.
Fig. S3. Device manufacture procedure that involves two steps: thermoforming and heat sealing.
Fig. S4. Test setup for force characterization and porous versus nonporous computational models.
Fig. S5. Analytical approximation for large deflection circular plate.
Fig. S6. Parametric study using large deflection plate analytical approximation.
Fig. S7. In vitro assessment of the effect of actuation of nonporous DSR on myofibroblast cell line (WPMY-1).
Fig. S8. Pre-clinical implementation of the DSRs.
Fig. S9. The dimensional effects of submerging the device, and its constituent material in saline with different concentrations.
Movie S1. Actuation of DSR with implantable pump.
Movie S2. Actuation of low profile nonporous DSR.
Movie S3. Actuation of DSR in vivo.
References (*62*, *63*)

REFERENCES AND NOTES

1. F. Lotti, F. Ranieri, G. Vadalà, L. Zollo, G. Di Pino, Invasive intraneural interfaces: Foreign body reaction issues. *Front. Neurosci.* **11**, 497 (2017).
2. T. D. Y. Kozai, A. S. Jaquins-Gerstl, A. L. Vazquez, A. C. Michael, X. T. Cui, Brain tissue responses to neural implants impact signal sensitivity and intervention strategies. *ACS Chem. Nerosci.* **6**, 48–67 (2014).
3. N. Cetin, N. M. Sav, E. Ciftci, B. Yildiz, Foreign body reaction to dialysis chatheter and peritoneal fluid eosinophilia in a child on continuous ambulatory peritoneal dialysis. *Iran. J. Kidney Dis.* **11**, 319–321 (2017).
4. X. Liu, L. Zhou, F. Pan, Y. Gao, X. Yuan, D. Fan, Comparison of the postoperative incidence rate of capsular contracture among different breast implants: A cumulative meta-analysis. *PLOS ONE* **10**, e0116071 (2015).
5. K. G. Tarakji, C. R. Ellis, P. Defaye, C. Kennergren, Cardiac implantable electronic device infection in patients at risk. *Arrhythmia Electrophysiol. Rev.* **5**, 65–71 (2016).
6. A. A. Sharkawy, B. Klitzman, G. A. Truskey, W. M. Reichert, Engineering the tissue which encapsulates subcutaneous implants. I. Diffusion properties. *J. Biomed. Mater. Res.* **37**, 401–412 (1997).
7. M. T. Novak, F. Yuan, W. M. Reichert, Modeling the relative impact of capsular tissue effects on implanted glucose sensor time lag and signal attenuation. *Anal. Bioanal. Chem.* **398**, 1695–1705 (2010).
8. V. Thomé-Duret, M. N. Gangnerau, Y. Zhang, G. S. Wilson, G. Reach, Modification of the sensitivity of glucose sensor implanted into subcutaneous tissue. *Diabetes Metab.* **22**, 174–178 (1996).
9. W. M. Fritschy, P. de Vos, H. Groen, F. A. Klatter, A. Pasma, G. H. J. Wolters, R. van Schilfgaarde, The capsular overgrowth on microencapsulated pancreatic islet grafts in streptozotocin and autoimmune diabetic rats. *Transpl. Int.* **7**, 264–271 (1994).
10. P. Soon-Shiong, M. Otterlie, G. Skjak-Braek, O. Smidsrod, R. Heintz, R. P. Lanza, T. Espevik, An immunologic basis for the fibrotic reaction to implanted microcapsules. *Transplant. Proc.* **23**, 758–759 (1991).
11. A. A. Sharkawy, B. Klitzman, G. A. Truskey, W. M. Reichert, Engineering the tissue which encapsulates subcutaneous implants. III. Effective tissue response times. *J. Biomed. Mater. Res. A* **40**, 598–605 (1998).
12. A. A. Sharkawy, B. Klitzman, G. A. Truskey, W. M. Reichert, Engineering the tissue which encapsulates subcutaneous implants. II. Plasma–tissue exchange properties. *J. Biomed. Mater. Res. A* **40**, 586–597 (1998).
13. *Global Opportunity Analysis and Industry Forecast 2014–2022* (Allied Market Research, 2018).
14. W. K. Ward, A review of the foreign-body response to subcutaneously-implanted devices: The role of macrophages and cytokines in biofouling and fibrosis. *J. Diab. Sci. Technol.* **2**, 768–777 (2008).
15. D. T. Luttikhuizen, M. C. Harmsen, M. J. A. Van Luyn, Cellular and molecular dynamics in the foreign body reaction. *Tissue Eng.* **12**, 1955–1970 (2006).
16. J. M. Anderson, K. Defife, A. McNally, T. Collier, C. Jenney, Monocyte, macrophage and foreign body giant cell interactions with molecularly engineered surfaces. *J. Mater. Sci. Mater. Med.* **10**, 579–588 (1999).
17. J. M. Anderson, A. Rodriguez, D. T. Chang, Foreign body reaction to biomaterials. *Semin. Immunol.* **20**, 86–100 (2008).
18. Y. M. Ju, B. Yu, L. West, Y. Moussy, F. Moussy, A dexamethasone-loaded PLGA microspheres/collagen scaffold composite for implantable glucose sensors. *J. Biomed. Mater. Res. A* **93**, 200–210 (2010).
19. A. Koh, S. P. Nichols, M. H. Schoenfisch, Glucose sensor membranes for mitigating the foreign body response. *J. Diabetes Sci. Technol.* **5**, 1052–1059 (2011).
20. R. J. Soto, B. J. Privett, M. H. Schoenfisch, In vivo analytical performance of nitric oxide-releasing glucose biosensors. *Anal. Chem.* **86**, 7141–7149 (2014).
21. R. J. Soto, E. P. Merricks, D. A. Bellinger, T. C. Nichols, M. H. Schoenfisch, Influence of diabetes on the foreign body response to nitric oxide-releasing implants. *Biomaterials* **157**, 76–85 (2018).
22. A. J. Vegas, O. Veiseh, M. Gürtler, J. R. Millman, F. W. Pagliuca, A. R. Bader, J. C. Doloff, J. Li, M. Chen, K. Olejnik, H. H. Tam, S. Jhunjhunwala, E. Langan, S. Aresta-Dasilva, S. Gandham, J. J. McGarrigle, M. A. Bochenek, J. Hollister-Lock, J. Oberholzer, D. L. Greiner, G. C. Weir, D. A. Melton, R. Langer, D. G. Anderson, Long-term glycemic control using polymer-encapsulated human stem cell–derived beta cells in immune-competent mice. *Nat. Med.* **22**, 306–311 (2016).

23. M. A. Bochenek, O. Veiseh, A. J. Vegas, J. J. McGarrigle, M. Qi, E. Marchese, M. Omami, J. C. Doloff, J. Mendoza-Elias, M. Nourmohammadzadeh, A. Khan, C.-C. Yeh, Y. Xing, D. Isa, S. Ghani, J. Li, C. Landry, A. R. Bader, K. Olejnik, M. Chen, J. Hollister-Lock, Y. Wang, D. L. Greiner, G. C. Weir, B. L. Strand, A. M. A. Rokstad, I. Lacik, R. Langer, D. G. Anderson, J. Oberholzer, Alginate encapsulation as long-term immune protection of allogeneic pancreatic islet cells transplanted into the omental bursa of macaques. *Nat. Biomed. Eng.* **2**, 810–821 (2018).
24. R. Robitaille, J.-F. Pariseau, F. A. Leblond, M. Lamoureux, Y. Lepage, J.-P. Hallé, Studies on small (< 350 μm) alginate-poly-L-lysine microcapsules. III. Biocompatibility of smaller versus standard microcapsules. *J. Biomed. Mater. Res.* **44**, 116–120 (1999).
25. O. Veiseh, J. C. Doloff, M. Ma, A. J. Vegas, H. H. Tam, A. R. Bader, J. Li, E. Langan, J. Wyckoff, W. S. Loo, S. Jhunjhunwala, A. Chiu, S. Siebert, K. Tang, J. Hollister-Lock, S. Aresta-Dasilva, M. Bochenek, J. Mendoza-Elias, Y. Wang, M. Qi, D. M. Lavin, M. Chen, N. Dholakia, R. Thakrar, I. Lacík, G. C. Weir, J. Oberholzer, D. L. Greiner, R. Langer, D. G. Anderson, Size- and shape-dependent foreign body immune response to materials implanted in rodents and non-human primates. *Nat. Mater.* **14**, 643–651 (2015).
26. B. F. Matlaga, L. P. Yasenchak, T. N. Salthouse, Tissue response to implanted polymers: The significance of sample shape. *J. Biomed. Mater. Res.* **10**, 391–397 (1976).
27. J. C. Doloff, O. Veiseh, A. J. Vegas, H. H. Tam, S. Farah, M. Ma, J. Li, A. Bader, A. Chiu, A. Sadraei, S. Aresta-Dasilva, M. Griffin, S. Jhunjhunwala, M. Webber, S. Siebert, K. Tang, M. Chen, E. Langan, N. Dholokia, R. Thakrar, M. Qi, J. Oberholzer, D. L. Greiner, R. Langer, D. G. Anderson, Colony stimulating factor-1 receptor is a central component of the foreign body response to biomaterial implants in rodents and non-human primates. *Nat. Mater.* **16**, 671–680 (2017).
28. Y. Ito, T. Kimura, Y. Ago, K. Nam, K. Hiraku, K. Miyazaki, T. Masuzawa, A. Kishida, Nano-vibration effect on cell adhesion and its shape. *Biomed. Mater. Eng.* **21**, 149–158 (2011).
29. G. A. Truskey, J. S. Pirone, The effect of fluid shear stress upon cell adhesion to fibronectin-treated surfaces. *J. Biomed. Mater. Res.* **24**, 1333–1353 (1990).
30. I. R. Titze, S. A. Klemuk, X. Lu, Adhesion of a monolayer of fibroblast cells to fibronectin under sonic vibrations in a bioreactor. *Ann. Otol. Rhinol. Laryngol.* **121**, 364–374 (2012).
31. M. E. Stamp, A. M. Jötten, P. W. Kudella, D. Breyer, F. G. Strobl, T. M. Geislinger, A. Wixforth, C. Westerhausen, Exploring the limits of cell adhesion under shear stress within physiological conditions and beyond on a chip. *Diagnostics* **6**, E38 (2016).
32. W. J. Kao, Evaluation of leukocyte adhesion on polyurethanes: The effects of shear stress and blood proteins. *Biomaterials* **21**, 2295–2303 (2000).
33. V. Ballotta, A. Driessen-Mol, C. V. C. Bouten, F. P. T. Baaijens, Strain-dependent modulation of macrophage polarization within scaffolds. *Biomaterials* **35**, 4919–4928 (2014).
34. C. A. Cezar, E. T. Roche, H. H. Vandenburgh, G. N. Duda, C. J. Walsh, D. J. Mooney, Biologic-free mechanically induced muscle regeneration. *Proc. Natl. Acad. Sci. U.S.A.* **113**, 1534–1539 (2016).
35. P. Polygerinos, N. Correll, S. A. Morin, B. Mosadegh, C. D. Onal, K. Petersen, M. Cianchetti, M. T. Tolley, R. F. Shepherd, Soft robotics: Review of fluid-driven intrinsically soft devices; manufacturing, sensing, control, and applications in human-robot interaction. *Adv. Eng. Mater.* **19**, 1700016 (2017).
36. E. T. Roche, M. A. Horvath, I. Wamala, A. Alazmani, S.-E. Song, W. Whyte, Z. Machaidze, C. J. Payne, J. C. Weaver, G. Fishbein, J. Kuebler, N. V. Vasilyev, D. J. Mooney, F. A. Pigula, C. J. Walsh, Soft robotic sleeve supports heart function. *Sci. Transl. Med.* **9**, eaaf3925 (2017).
37. M. A. Horvath, C. E. Varela, E. B. Dolan, W. Whyte, D. S. Monahan, C. J. Payne, I. A. Wamala, N. V. Vasilyev, F. A. Pigula, D. J. Mooney, C. J. Walsh, G. P. Duffy, E. T. Roche, Towards alternative approaches for coupling of a soft robotic sleeve to the heart. *Ann. Biomed. Eng.* **46**, 1534–1547 (2018).
38. M. A. Horvath, I. Wamala, E. Rytkin, E. Doyle, C. J. Payne, T. Thalhofer, I. Berra, A. Solovyeva, M. Saeed, S. Hendren, E. T. Roche, P. J. del Nido, C. J. Walsh, N. V. Vasilyev, An intracardiac soft robotic device for augmentation of blood ejection from the failing right ventricle. *Ann. Biomed. Eng.* **45**, 2222–2233 (2017).
39. W. Whyte, E. T. Roche, C. E. Varela, K. Mendez, S. Islam, H. O'Neill, F. Weafer, R. N. Shirazi, J. C. Weaver, N. V. Vasilyev, P. E. McHugh, B. Murphy, G. P. Duffy, C. J. Walsh, D. J. Mooney, Sustained release of targeted cardiac therapy with a replenishable implanted epicardial reservoir. *Nat. Biomed. Eng.* **2**, 416–428 (2018).
40. C. Howard, M. Reed, *Unbiased Stereology: Three-Dimensional Measurement in Microscopy* (QTP Publications, 2010).
41. E. B. Jensen, H. J. G. Gundersen, The stereological estimation of moments of particle volume. *J. Appl. Probab.* **22**, 82–98 (1985).
42. P. Dockery, J. Fraher, The quantification of vascular beds: A stereological approach. *Exp. Mol. Pathol.* **82**, 110–120 (2007).
43. N. N. Madigan, B. K. Chen, A. M. Knight, G. E. Rooney, E. Sweeney, L. Kinnavane, M. J. Yaszemski, P. Dockery, T. O'Brien, S. S. McMahon, A. J. Windebank, Comparison of cellular architecture, axonal growth, and blood vessel formation through cell-loaded polymer scaffolds in the transected rat spinal cord. *Tissue Eng. Part A* **20**, 2985–2997 (2014).
44. B. D. Ratner, Reducing capsular thickness and enhancing angiogenesis around implant drug release systems. *J. Control. Release* **78**, 211–218 (2002).
45. J. D. Bryers, C. M. Giachelli, B. D. Ratner, Engineering biomaterials to integrate and heal: The biocompatibility paradigm shifts. *Biotechnol. Bioeng.* **109**, 1898–1911 (2012).
46. S. van Putten, Y. Shafieyan, B. Hinz, Mechanical control of cardiac myofibroblasts. *J. Mol. Cell. Cardiol.* **93**, 133–142 (2016).
47. M. E. Blaauboer, T. H. Smit, R. Hanemaaijer, R. Stoop, V. Everts, Cyclic mechanical stretch reduces myofibroblast differentiation of primary lung fibroblasts. *Biochem. Biophys. Res. Commun.* **404**, 23–27 (2011).
48. L. A. Taber, Biomechanics of cardiovascular development. *Annu. Rev. Biomed. Eng.* **3**, 1–25 (2001).
49. P. Patwari, R. T. Lee, Mechanical control of tissue morphogenesis. *Circ. Res.* **103**, 234–243 (2008).
50. E. Dolgin, Diabetes: Encapsulating the problem. *Nature* **540**, S60–S62 (2016).
51. E. Dolgin, Encapsulate this. *Nat. Med.* **20**, 9–11 (2014).
52. L. Xu, S. R. Gutbrod, A. P. Bonifas, Y. Su, M. S. Sulkin, N. Lu, H.-J. Chung, K.-I. Jang, Z. Liu, M. Ying, C. Lu, R. C. Webb, J.-S. Kim, J. I. Laughner, H. Cheng, Y. Liu, A. Ameen, J.-W. Jeong, G.-T. Kim, Y. Huang, I. R. Efimov, J. A. Rogers, 3D multifunctional integumentary membranes for spatiotemporal cardiac measurements and stimulation across the entire epicardium. *Nat. Commun.* **5**, 3329 (2014).
53. M. Kubon, H. Hartmann, M. Moschallski, C. Burkhardt, G. Link, S. Werner, P. Lavalle, G. Urban, N. E. Vrana, M. Stelzle, Multimodal chemosensor-based, real-time biomaterial/cell interface monitoring. *Adv. Biosys.* **2**, 1700236 (2018).
54. S. H. Lee, Y. B. Lee, B. H. Kim, C. Lee, Y. M. Cho, S.-N. Kim, C. G. Park, Y.-C. Cho, Y. B. Choy, Implantable batteryless device for on-demand and pulsatile insulin administration. *Nat. Commun.* **8**, 15032 (2017).
55. J. Kim, G. A. Salvatore, H. Araki, A. M. Chiarelli, Z. Xie, A. Banks, X. Sheng, Y. Liu, J. W. Lee, K.-I. Jang, S. Y. Heo, K. Cho, H. Luo, B. Zimmerman, J. Kim, L. Yan, X. Feng, S. Xu, M. Fabiani, G. Gratton, Y. Huang, U. Paik, J. A. Rogers, Battery-free, stretchable optoelectronic systems for wireless optical characterization of the skin. *Sci. Adv.* **2**, e1600418 (2016).
56. B. Lu, Y. Chen, D. Ou, H. Chen, L. Diao, W. Zhang, J. Zheng, W. Ma, L. Sun, X. Feng, Ultra-flexible piezoelectric devices integrated with heart to harvest the biomechanical energy. *Sci. Rep.* **5**, 16065 (2015).
57. E. B. Dolan, L. Kovarova, H. O'Neill, M. Pravda, R. Sulakova, I. Scigalkova, V. Velebny, D. Daro, N. Braun, G. M. Cooney, G. Bellavia, S. Straino, B. L. Cavanagh, A. Flanagan, H. M. Kelly, G. P. Duffy, B. P. Murphy, Advanced Material Catheter (AMCath), a minimally invasive endocardial catheter for the delivery of fast-gelling covalently cross-linked hyaluronic acid hydrogels. *J. Biomater. Appl.* **33**, 681–692 (2018).
58. M. G. Monaghan, M. Holeiter, E. Brauchle, S. L. Layland, Y. Lu, A. Deb, A. Pandit, A. Nsair, K. Schenke-Layland, Exogenous miR-29B delivery through a hyaluronan-based injectable system yields functional maintenance of the infarcted myocardium. *Tissue Eng. Part A* **24**, 57–67 (2018).
59. E. B. Dolan, B. Hofmann, M. H. de Vaal, G. Bellavia, S. Straino, L. Kovarova, M. Pravda, V. Velebny, D. Daro, N. Braun, D. S. Monahan, R. E. Levey, H. O'Neill, S. Hinderer, R. Greensmith, M. G. Monaghan, K. Schenke-Layland, P. Dockery, B. P. Murphy, H. M. Kelly, S. Wildhirt, G. P. Duffy, A bioresorbable biomaterial carrier and passive stabilization device to improve heart function post-myocardial infarction. *Mater. Sci. Eng. C* **103**, 109751 (2019).
60. J. C. F. De Winter, Using the Student's *t*-test with extremely small sample sizes. *Pract. Assess. Res. Eval.* **18**, 10 (2013).
61. K.-Y. Liang, S. L. Zeger, Longitudinal data analysis using generalized linear models. *Biometrika* **73**, 13–22 (1986).
62. Y. Zhang, Large deflection of clamped circular plate and accuracy of its approximate analytical solutions. *Sci. China Phys. Mech. Astron.* **59**, 624602 (2016).
63. S. Timoshenko, S. Woinowsky-Krieger, *Theory of Plates and Shells* (McGraw-Hill Book Company, 1959).

Acknowledgments: We acknowledge the support of the Centre of Microscopy and Imaging (NUI Galway) and the Koch Imaging Core (MIT) for imaging expertise. We also thank M. Canney, K. Thompson, and D. Connolly for imaging technical support and T. Fresneau, M. Horvath, R. O'Connor, J. Murphy, J. Hardin, and J. Prendergast for research assistance. **Funding:** E.T.R. acknowledges funding from the Mechanical Engineering Department and the Institute for Medical Engineering and Science at the Massachusetts Institute of Technology. W.W., S.T.R., and G.P.D. acknowledge funding from Science Foundation Ireland under grant SFI/12/RC/2278, Advanced Materials and Bioengineering Research (AMBER) Centre, National University of Ireland and Trinity College Dublin, Ireland. G.P.D., R.E.L., and E.M. acknowledge financial support from the National University of Ireland Galway. E.B.D. and G.P.D. acknowledge The DRIVE project, which has received funding from the European Union's Horizon 2020 research and innovation program under grant agreement number 645991. E.B.D. and G.P.D. acknowledge funding from the European Molecular Biology Organization Short-Term Fellowship. S.T.R. has received funding from the European Union's Horizon 2020

research and innovation program under the Marie Skłodowska-Curie grant agreement no. 713567. A.R. acknowledges funding from the Harvard College Research Program (HCRP). C.E.V. acknowledges the financial support from the National Science Foundation Graduate Research Fellowship Program. Any opinions, findings, and conclusions or recommendations expressed in this material are those of the author(s) and do not necessarily reflect the views of the National Science Foundation. This work was conducted with support from Harvard Catalyst | The Harvard Clinical and Translational Science Center (National Center for Advancing Translational Sciences, National Institutes of Health Award UL 1TR002541) and financial contributions from Harvard University and its affiliated academic health care centers. The content is solely the responsibility of the authors and does not necessarily represent the official views of Harvard Catalyst, Harvard University and its affiliated academic health care centers, or the National Institutes of Health.

Author contributions: E.B.D., C.E.V., K.M., W.W., S.T.R., P.D., G.P.D., and E.T.R. designed the study. E.B.D., C.E.V., K.M., W.W., R.E.L., J.O., R.B., A.R., J.H., S.T.R., S.E.R., E.M., Y.F., R.W., and M.M. performed the experiments. E.B.D., C.E.V., K.M., W.W., S.T.R., R.E.L., E.M., J.R.S., Y.F., M.M., G.P.D., and E.T.R. analyzed and reviewed the data. E.B.D., C.E.V., K.M., S.T.R., G.P.D., and E.T.R. wrote the manuscript. All authors reviewed and edited the manuscript. **Competing interests:** G.P.D. has received consultancy payments from Boston Scientific. E.B.D., G.P.D., K.M., S.T.R., S.E.R., E.T.R., C.E.V., and W.W. are inventors on a pending patent application. **Data and materials availability:** All data needed to evaluate the conclusions in the paper are present in the paper or the Supplementary Materials. Devices can be obtained through a material transfer agreement.

Submitted 15 April 2019
Accepted 1 August 2019
Published 28 August 2019
10.1126/scirobotics.aax7043

Citation: E. B. Dolan, C. E. Varela, K. Mendez, W. Whyte, R. E. Levey, S. T. Robinson, E. Maye, J. O'Dwyer, R. Beatty, A. Rothman, Y. Fan, J. Hochstein, S. E. Rothenbucher, R. Wylie, J. R. Starr, M. Monaghan, P. Dockery, G. P. Duffy, E. T. Roche, An actuatable soft reservoir modulates host foreign body response. *Sci. Robot.* **4**, eaax7043 (2019).

Science Robotics

An actuatable soft reservoir modulates host foreign body response

E. B. Dolan, C. E. Varela, K. Mendez, W. Whyte, R. E. Levey, S. T. Robinson, E. Maye, J. O'Dwyer, R. Beatty, A. Rothman, Y. Fan, J. Hochstein, S. E. Rothenbucher, R. Wylie, J. R. Starr, M. Monaghan, P. Dockery, G. P. Duffy, and E. T. Roche

Sci. Robot. **4** (33), eaax7043. DOI: 10.1126/scirobotics.aax7043

Science Robotics (ISSN 2470-9476) is published by the American Association for the Advancement of Science. 1200 New York Avenue NW, Washington, DC 20005. The title *Science Robotics* is a registered trademark of AAAS.